REPORT

CHEMICAL GENETICS

IFITM proteins assist cellular uptake of diverse linked chemotypes

Kevin Lou[1,2], Douglas R. Wassarman[1,2], Tangpo Yang[1], YiTing Paung[3], Ziyang Zhang[1,2,4], Thomas A. O'Loughlin[5,6], Megan K. Moore[1,2], Regina K. Egan[7], Patricia Greninger[7], Cyril H. Benes[7,8], Markus A. Seeliger[3], Jack Taunton[1], Luke A. Gilbert[5,6,9,10]*, Kevan M. Shokat[1,2,4]*

The search for cell-permeable drugs has conventionally focused on low-molecular weight (MW), nonpolar, rigid chemical structures. However, emerging therapeutic strategies break traditional drug design rules by employing flexibly linked chemical entities composed of more than one ligand. Using complementary genome-scale chemical-genetic approaches we identified an endogenous chemical uptake pathway involving interferon-induced transmembrane proteins (IFITMs) that modulates the cell permeability of a prototypical biopic inhibitor of MTOR (RapaLink-1, MW: 1784 g/mol). We devised additional linked inhibitors targeting BCR-ABL1 (DasatiLink-1, MW: 1518 g/mol) and EIF4A1 (BisRoc-1, MW: 1466 g/mol), uptake of which was facilitated by IFITMs. We also found that IFITMs moderately assisted some proteolysis-targeting chimeras and examined the physicochemical requirements for involvement of this uptake pathway.

Any therapeutic molecule that binds to an intracellular target must first cross the cell membrane. Retrospective analyses of compound libraries and their biological activities have yielded empirical guidelines (e.g., Lipinski's rule of five) that enrich for lead-like scaffolds with high passive permeability and largely define modern drug-like chemical space (*1*–*3*). Although these principles have been useful for streamlining the search for new therapeutics, many important intracellular drug targets are currently refractory to inhibition by these compact, hydrophobic, and rigid molecules. One emerging design framework that seeks to address these challenges involves increasing pharmacological complexity by linking multiple ligands into a single chemical entity (a linked chemotype). Linked chemotypes can have enhanced potency, greater selectivity, and the capacity to induce the association of more than one target (*4*–*11*). This modular rapid access to high molecular weight, amphiphilicity, and rotational flexibility can provide useful chemical probes and therapeutic leads for intracellular targets, as long as the resulting molecules remain cell-permeable.

Mechanisms to understand and predict the cell permeability of linked chemotypes, however, remain limited. Other medium-to-high molecular weight therapeutics such as natural products and synthetic macrocycles often constitute highly tailored arrangements of polar and nonpolar functionality that allow switching between membrane-favored and aqueous-favored conformations to enable passive permeability through membranes (*12*). Additionally, cell-penetrating proteins/peptides commonly require appendage of highly charged moieties to enable electrostatic interactions with the plasma membrane and subsequent internalization (*13*–*15*). Studies involving the most rapidly expanding linked chemotype class—proteolysis-targeting chimeras (PROTACs) (*16*)—provide varying insights into the determinants of cell permeability (*17*–*22*). Despite their atypical properties, PROTACs and additional large molecules such as the dimeric immunophilin ligand rimiducid have shown in-cell activity robust enough to enter clinical trials (*16*, *23*).

Given this discrepancy between the favorable biological activity of many large, bivalent molecules and traditional concepts of passive permeability, we inferred that linked chemotypes might hijack cellular processes to assist with passage through the cell membrane. We selected as an example a bitopic inhibitor of MTOR, RapaLink-1 (*7*), whose molecular weight (1784 g/mol) falls well beyond common guidelines (≤ 500 g/mol) (*1*), and even beyond that of typical PROTACs (800 to 1200 g/mol) (table S1) (*18*). RapaLink-1's atypical structure—composed of the allosteric MTOR inhibitor rapamycin and the active site inhibitor sapanisertib linked by an 8-unit polyethylene glycol (PEG8) tether (Fig. 1A)—confers enhanced selectivity for MTOR complex 1 over MTOR complex 2 (*7*, *24*, *25*). The molecule is highly active in vivo, penetrates the blood-brain barrier, and serves as a prototype for the clinical candidate RMC-5552 (*7*, *24*–*27*), establishing itself as a drug-like compound that defies most traditional notions of drug-like structures. We hypothesized that cellular mechanisms assisting RapaLink-1's cytoplasmic entry could be identified by systematically perturbing genes that modulate the molecule's ability to reach and inhibit its intracellular target.

Complementary genome-scale chemical-genetic approaches identify IFITMs as regulators of RapaLink-1 cellular activity

We probed canonical protein-coding genes for cellular factors that determine RapaLink-1 uptake and sensitivity using a dCas9-based CRISPRi/a functional genomics platform (*28*, *29*). Gene expression inhibition and activation, through CRISPRi and CRISPRa, respectively, act as complementary approaches to map chemical-genetic interactions at the genome scale. In particular, genes displaying strong mirrored phenotypes (resistance upon knockdown and sensitivity upon overexpression) are likely to be directly involved in a small molecule's mechanism of action. This integrated approach to identifying physiologically relevant chemical-genetic interactions was proposed by Jost *et al*. and its utility has recently been reviewed (*30*, *31*). In addition to the bitopic inhibitor, we also assessed sapanisertib, rapamycin, and an unlinked control (a 1:1 mixture of sapanisertib and rapamycin) to distinguish chemical-genetic interactions specific to the linked chemotype (Fig. 1A).

Patient-derived chronic myeloid leukemia (CML) cells, K562, pre-engineered to express CRISPRi or CRISPRa machinery, were transduced with their respective genome-scale sgRNA libraries, selected with puromycin to remove nontransduced cells, and treated with DMSO, sapanisertib, rapamycin, sapanisertib + rapamycin, or RapaLink-1. The experiments were conducted with high-replicate reproducibility (fig. S1, A to D), and data from the genome-scale CRISPRi (data S1 and S2) and CRISPRa (data S3 and S4) screens were juxtaposed to highlight genes that displayed mirrored phenotypes (Fig. 1B). This arrangement distributes genes which functionally synergize with the inhibitor in the lower right (e.g., *FKBP12*, the required inhibitory complex partner of rapamycin) and those which antagonize the inhibitor in the upper left (e.g., *MTOR*, the direct target) (*30*, *31*). Chemical-genetic

[1]Department of Cellular and Molecular Pharmacology, University of California, San Francisco, San Francisco, CA 94158, USA. [2]Howard Hughes Medical Institute, University of California, San Francisco, San Francisco, CA 94158, USA. [3]Department of Pharmacological Sciences, Stony Brook University, Stony Brook, NY 11794-8651, USA. [4]Department of Chemistry, University of California, Berkeley, Berkeley, CA 94720, USA. [5]Helen Diller Family Comprehensive Cancer Center, University of California, San Francisco, San Francisco, CA 94158, USA. [6]Department of Urology, University of California, San Francisco, San Francisco, CA 94158, USA. [7]Center for Cancer Research, Massachusetts General Hospital Cancer Center, Charlestown, MA 02129, USA. [8]Department of Medicine, Harvard Medical School, Boston, MA 02115, USA. [9]Innovative Genomics Institute, University of California, San Francisco, San Francisco, CA 94158, USA. [10]Arc Institute, Palo Alto, CA 94304, USA.
*Corresponding author. Email: kevan.shokat@ucsf.edu (K.M.S.); luke@arcinstitute.org (L.A.G.)

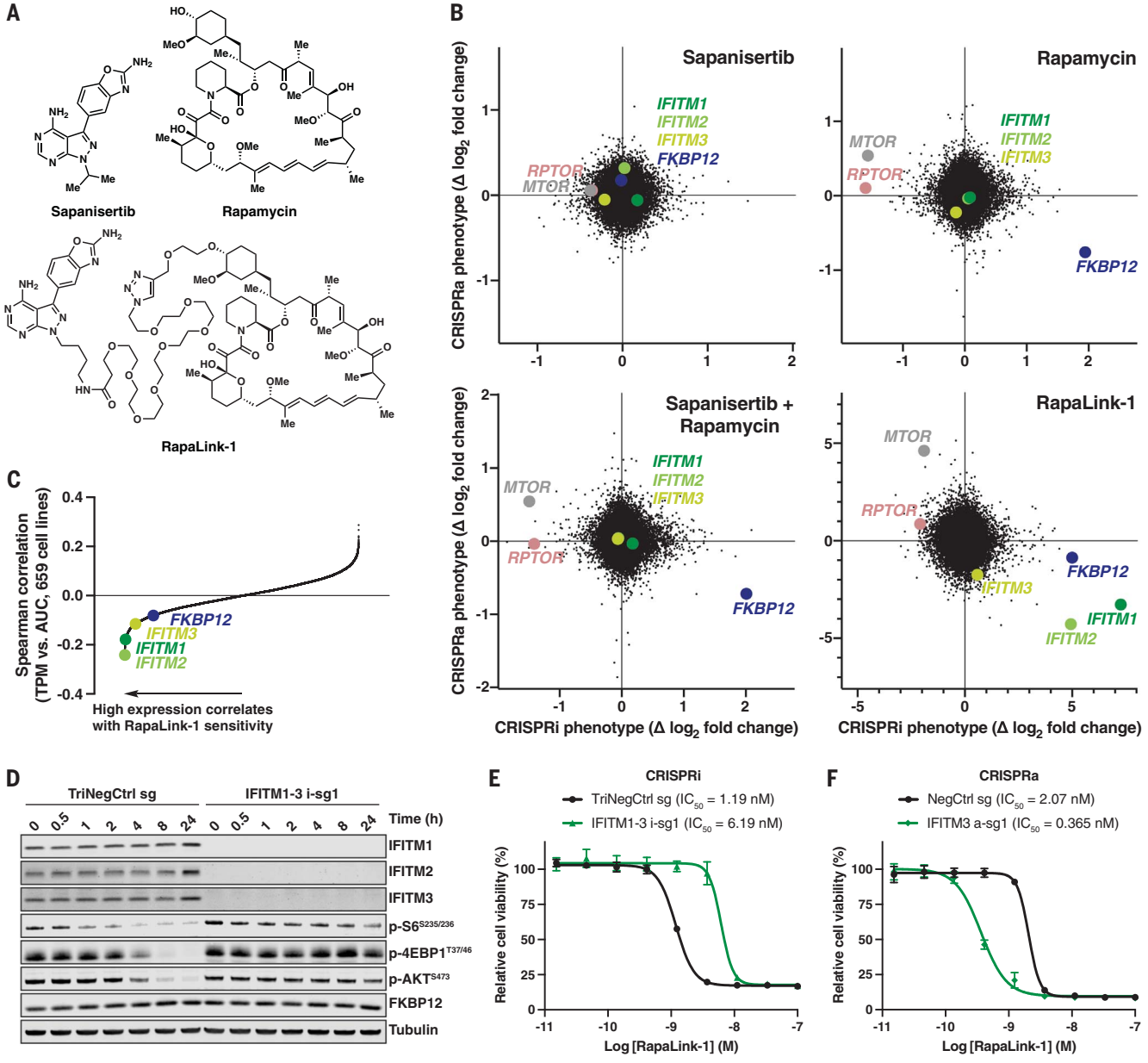

Fig. 1. IFITMs promote the cellular activity of a bitopic MTOR inhibitor. (**A**) Chemical structures of MTOR inhibitors. (**B**) Gene phenotypes from genome-scale CRISPRi and CRISPRa screens in K562 cells. Genes involved in MTOR complex 1 (*MTOR* and *RPTOR*), a requisite rapamycin inhibitory complex partner (*FKBP12*), and clade I IFITMs (*IFITM1*, *IFITM2*, and *IFITM3*) are highlighted. Data represent two biological replicates. (**C**) Spearman correlation coefficients between RapaLink-1 sensitivity, as measured by dose-response data, and transcript abundance, as measured by RNA sequencing (see also fig. S4). Dose-response data are expressed as area under the curve (AUC) and RNA sequencing data are expressed as transcripts per million (TPM). Genes are highlighted as in (B). (**D**) Immunoblots of K562 CRISPRi cells expressing sgRNAs treated with RapaLink-1 (3 nM) for the times indicated. [(**E**) and (**F**)] Viability of K562 CRISPRi (E) or CRISPRa (F) cells expressing sgRNAs treated with RapaLink-1. Data represent means of three biological replicates; error bars denote SD.

interactions with MTOR signaling components, particularly the Ragulator complex (*RRAGA*, *RRAGC*, and *LAMTOR1-5*) and nodes downstream of PI3K/AKT (*TSC1*, *TSC2*, and *RHEB*), were observed across multiple inhibitor conditions (fig. S2, A and B), consistent with known pathway relationships (*32*) and prior functional genomics studies (*33*, *34*).

A distinct set of chemical-genetic interactions were identified as top hits with RapaLink-1 and not with any of the nonlinked molecules tested, suggesting the involvement of a biological pathway that promotes the activity of the linked chemotype. The expression of members of a highly homologous gene family—interferon-induced transmembrane proteins (IFITMs) *IFITM1*, *IFITM2*, and *IFITM3* (*35*)—synergized with the activity of RapaLink-1 and not its nonlinked counterparts, sapanisertib and rapamycin (Fig. 1B). To validate this finding, we tested sgRNAs targeting *IFITM1-3* individually for transcriptional repression or activation (fig. S3A and table S2). CRISPRi-mediated knockdown of *IFITM1-3* was potent and selective (fig. S3B). CRISPRa-mediated overexpression was also potent although we observed variable cross activation between family members (fig. S3C), possibly due to concerted transcriptional regulation of these genes, which are adjacent to each other on

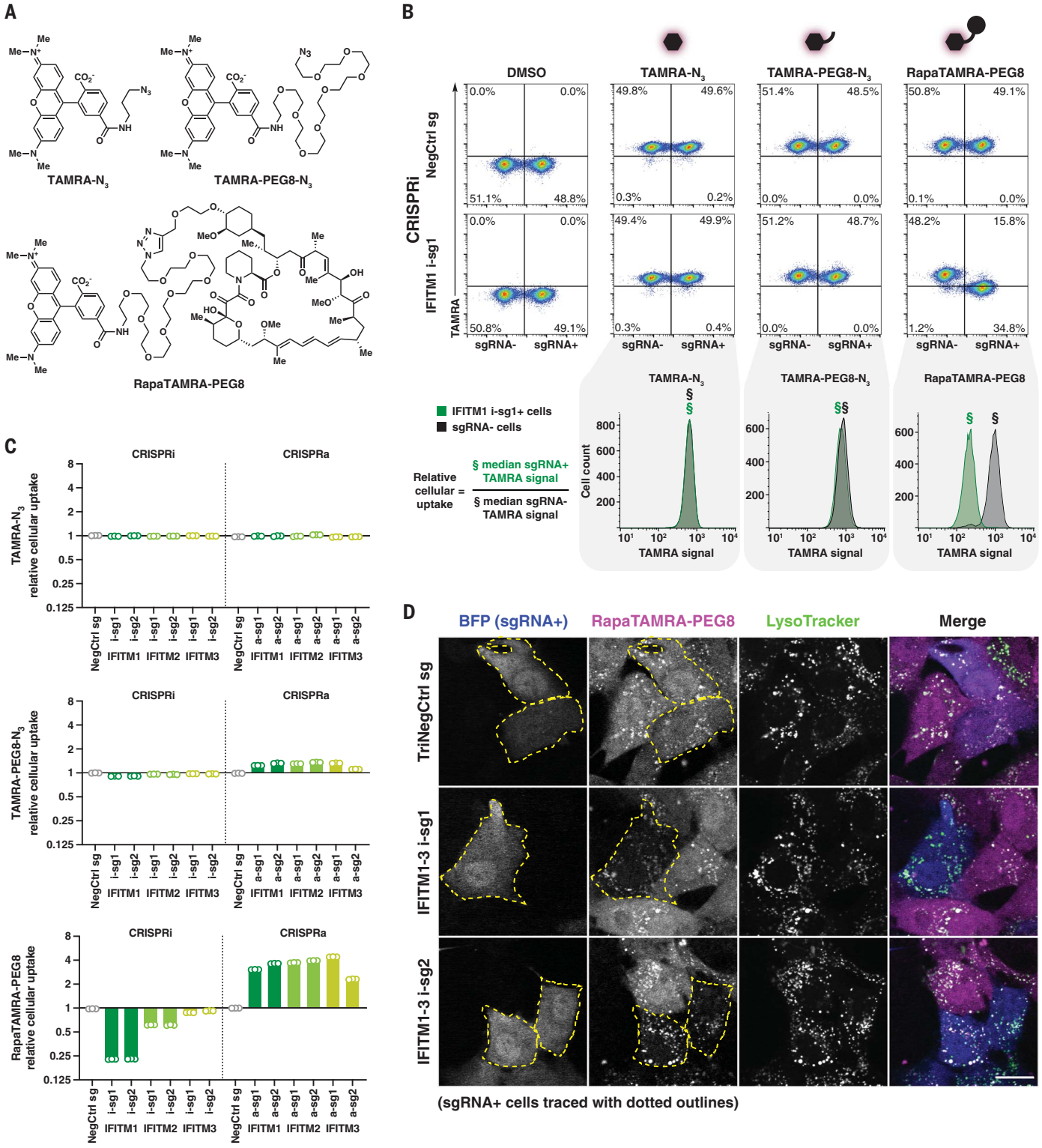

Fig. 2. IFITMs promote the cellular uptake of linked chemotypes. (**A**) Chemical structures of fluorescent RapaLink-1 analogs. (**B**) Measurement of fluorescent molecule uptake in K562 CRISPRi cells expressing sgRNAs (sgRNA+). Cells were incubated with TAMRA-N_3 (10 nM), TAMRA-PEG8-N_3 (1 μM), or RapaTAMRA-PEG8 (1 nM) for 24 hours. Uptake modulation by sgRNAs was quantified by internal normalization to nontransduced cells (sgRNA-) present within the mixture (i.e., relative cellular uptake). Data representative of three biological replicates. (**C**) Changes in uptake of fluorescent molecules by sgRNAs targeting *IFITM1-3* as in (B) and fig. S6A. Relative cellular uptake <1 indicates decreased uptake and >1 indicates increased uptake. Data represent means of three biological replicates. (**D**) Confocal microscopy images of RPE-1 CRISPRi cells expressing indicated sgRNAs (blue) and treated for 24 hours with RapaTAMRA-PEG8 (magenta) and LysoTracker (green). sgRNA+ cells are traced with dotted outlines (yellow) in left two columns for clarity. Scale bar denotes 20 μm.

chromosome 11 (fig. S3A) (*36*). We individually confirmed that top screen hits, including *FKBP12* and *IFITM1-3*, synergized with RapaLink-1 in a competitive growth assay; we also validated that the *IFITM1-3* chemical-genetic interaction was specific to the linked chemotype (fig. S3, D and E).

Seeking to generalize these observations beyond a single cell type, we employed an independent chemical-genetic approach correlating MTOR inhibitor sensitivity data with basal gene expression in diverse in vitro models (*37*–*39*). More than 500 cancer cell lines were assessed for sensitivity to sapanisertib, rapamycin, or RapaLink-1 (measured by area under the dose-response curve). These measurements were correlated with gene transcript abundance (measured by RNA sequencing) across the cell lines to identify predictive biomarkers for compound sensitivity or resistance. High expression of any of the three IFITM family members was strongly associated with enhanced RapaLink-1 sensitivity across 659 cell lines, and *IFITM2* was notably the single most associated sensitizing biomarker (negative correlation) for Rapalink-1 (Fig. 1C and data S5). This correlation was absent for sapanisertib and rapamycin (fig. S4, A to C, and data S5), recapitulating the CRISPRi/a screens. Together, our analysis of the CRISPRi/a screens and large-scale chemogenomic cell line profiling experiments suggested a role of IFITMs in promoting the activity of RapaLink-1 across diverse cell types and levels of IFITM expression.

IFITMs promote RapaLink-1 pharmacodynamic target engagement

To unmask potentially overlapping IFITM functions, we knocked down *IFITM1*, *IFITM2*, and *IFITM3* expression simultaneously by coexpressing three different targeting sgRNAs (table S2) (*40*). Although multigene knockdown was potent (fig. S5A), we did not observe baseline changes in cell viability (fig. S5B). *IFITM1-3* triple knockdown ablated MTOR inhibition by 3 nM RapaLink-1 in cells, as determined by intracellular markers of MTOR pathway signaling, phospho-S6$^{S235/236}$, phospho-4EBP1$^{T37/46}$, and phospho-AKT^{S473} (Fig. 1D), and conferred resistance to the linked molecule (Fig. 1E and fig. S5C). Overall, IFITM expression perturbation by CRISPRi and CRISPRa caused a combined 29.5-fold modulation in cellular potency of the molecule (Fig. 1, E and F). As observed previously (*7*), RapaLink-1 requires multiple hours to achieve maximal pharmacodynamic inhibition (Fig. 1D). This contrasts with the typical finding that small molecules reach their intracellular targets on a timescale of seconds to minutes (*41*) and may reflect how linked chemotypes exhibit distinct permeability characteristics from traditional drug-like molecules.

Neither of the nonlinked MTOR inhibitors tested demonstrated chemical-genetic interactions with *IFITM1-3* and thus IFITMs likely do not directly modulate MTOR signaling but instead cooperate with some aspect of RapaLink-1 not shared with the other inhibitors. Clade I IFITM family members, *IFITM1-3*, are closely related broad spectrum viral restriction factors that localize to the plasma and endolysosomal membranes (*42*–*45*). They are thought to perform their antiviral function in part by rendering local membrane characteristics at the viral-endosomal juncture unfavorable for viral entry (*46*), although in some cases viruses can also hijack IFITMs to facilitate entry and infection (*47*). In addition to their established immunologic function, clade I IFITMs are also reported to modulate an oncogenic phenotype (*48*), affect placenta formation (*49*), and contribute to cellular homeostasis (*44*). In turn, Rapalink-1 might interact with IFITMs through a cellular pathway that promotes uptake of large molecules.

A fluorescent RapaLink-1 analog reveals a role for IFITMs in linked chemotype uptake

To explore our uptake hypothesis, we created a fluorescent analog of RapaLink-1 to directly observe the effect of IFITM expression on accumulation of the linked chemotype in live cells. This fluorescent molecule, RapaTAMRA-PEG8, was designed by replacing the adenosine triphosphate (ATP)-site binding element in RapaLink-1 with tetramethylrhodamine (TAMRA), resulting in a fluorescent derivative that closely mimics the physicochemical properties of the original molecule (Fig. 2A and table S1) (*27*). Analogs representing partial components of RapaTAMRA-PEG8, TAMRA-N_3, and TAMRA-PEG8-N_3, were additionally evaluated to assess whether the uptake pathway extended to generic compact-hydrophobic or linked-amphiphilic chemotypes respectively (Fig. 2A). We quantified accumulation of these molecules by flow cytometry using a quantitative live cell fluorescence uptake assay in which a mixture of transduced (sgRNA$^+$) and nontransduced (sgRNA$^-$) cells were equally exposed to compounds within the same well (Fig. 2B and fig. S6A). Changes in cellular uptake resulting from CRISPRi/a expression modulation by sgRNAs (fig. S3, A to C) again revealed a chemotype-specific IFITM dependency pattern (Fig. 2, B and C, and fig. S6A). Both linked chemotypes—TAMRA-PEG8-N_3 and RapaTAMRA-PEG8—demonstrated decreased uptake upon knockdown of *IFITM1-3* and increased uptake upon overexpression. The linker-less chemotype TAMRA-N_3, by contrast, exhibited no such chemical-genetic interactions. CRISPRi/a-induced uptake differences observed for RapaTAMRA-PEG8 correlated strongly with resistance and sensitivity phenotypes for RapaLink-1 (fig. S6B), suggesting a direct association between measured uptake and functional target inhibition. The observation that uptake of TAMRA-PEG8-N_3—a generic linked chemotype not specifically bound by any cellular protein—was also IFITM-assisted suggests that this uptake mechanism might also be used by other linked molecules.

Additionally, we assessed the role of IFITMs on the subcellular localization of RapaTAMRA-PEG8 by confocal microscopy in a human nontransformed cell line, RPE-1, pre-engineered to express CRISPRi machinery. Again a mixture of sgRNA$^+$ and sgRNA$^-$ cells were imaged in the same well following equal exposure to the fluorescent compound. *IFITM1-3* triple-knockdown significantly reduced the amount of RapaTAMRA-PEG8 entering the intracellular compartment (Fig. 2D and fig. S6C). A reduction in signal was also observed within the endolysosomal compartment (Fig. 2D and fig. S6C), suggesting that IFITMs, which localize to the plasma membrane as well as to endolysosomal membranes (*43*–*45*), may play a role in facilitating RapaTAMRA-PEG8 uptake through endocytic vesicles and into the intracellular space. Consistent with this, our functional genomics screens identified RapaLink-1–specific chemical-genetic interactions among endosomal (*ARF6*, *VPS26A*, *VPS29*, and *VPS35*) and sterol (*OSBP*, *GRAMD1A*, *INSIG1*, and *SCAP*) regulatory genes (fig. S7, A and B). This, in part, resembles the role IFITMs play as antiviral effectors in which biophysical interactions with incoming viral particles (*50*) and membrane sterols (*51*) may hinder or assist infection of target cells (*43*–*45*). Considering the large diversity of viruses IFITMs are described to interact with, we hypothesized that the uptake assistance afforded to RapaLink-1 and RapaTAMRA-PEG8 by IFITMs might also extend to other linked chemotypes with similar physicochemical properties.

DasatiLink-1 is an IFITM-assisted bitopic inhibitor of BCR-ABL1 with enhanced selectivity

To explore the generalizability of this IFITM-promoted cellular uptake mechanism, we designed, synthesized, and characterized a bitopic inhibitor that is, aside from being a linked molecule, compositionally unrelated to RapaLink-1. This inhibitor targets a different intracellular protein, BCR-ABL1, a fusion oncoprotein associated with CML and other leukemias (*52*). BCR-ABL1 harbors two well-defined small-molecule binding sites within its kinase domain (Fig. 3A): the ATP pocket (*53*), which is targeted by five clinically approved compounds (e.g., dasatinib) (*54*), and the myristoyl pocket (*55*), which is targeted by the clinical inhibitor asciminib (*56*). These sites can also be bound by the two classes of inhibitors simultaneously (*55*–*57*). The two pockets span a distance similar to that engaged by RapaLink-1 in MTOR

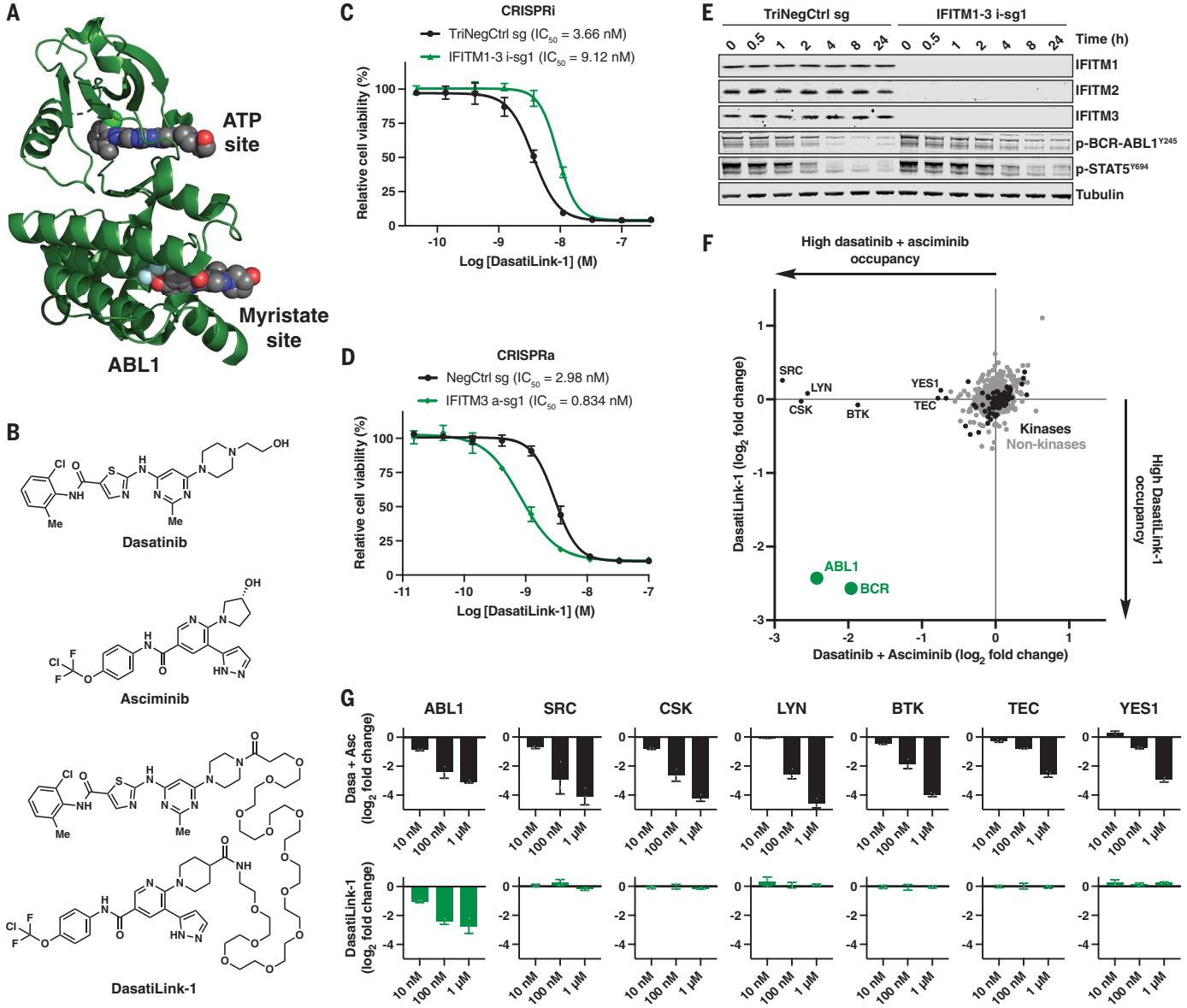

Fig. 3. Design and characterization of an IFITM-assisted bitopic BCR-ABL1 inhibitor. (**A**) Molecular model of ABL1 kinase domain. The model was constructed by aligning two crystal structures: one bound to dasatinib (PDB, 2GQG) and one bound to asciminib (PDB, 5MO4). (**B**) Chemical structures of BCR-ABL1 inhibitors. [(**C**) and (**D**)] Viability of K562 CRISPRi (C) or CRISPRa (D) cells expressing sgRNAs treated with DasatiLink-1. Data represent means of three biological replicates; error bars denote SD. (**E**) Immunoblots of K562 CRISPRi cells expressing sgRNAs treated with DasatiLink-1 (5 nM) for the times indicated (**F**) In-cell kinase occupancy profiling of DasatiLink-1 and an unlinked control (a 1:1 mixture of dasatinib and asciminib) at equimolar concentration (100 nM). Data represent means of three biological replicates. (**G**) As in (F) for kinases occupied following 10 nM, 100 nM, and 1 μM inhibitor treatments; error bars denote SD.

(*7*), suggesting that a similar bitopic inhibitor linkage strategy could apply to BCR-ABL1. We devised a bitopic inhibitor of BCR-ABL1, DasatiLink-1, based on the linking of dasatinib and asciminib by a flexible tether whose length (41 heavy atoms) was close to that of RapaLink-1 (39 heavy atoms) (Fig. 3B).

We characterized the interaction between DasatiLink-1 and its target using in vitro biochemical assays. Treatment of purified BCR-ABL1 kinase domain with dasatinib or asciminib resulted in marked (>0.1 ppm) nuclear magnetic resonance (NMR) chemical shift differences in residues involved in binding to the monomeric inhibitors (fig. S8, A and B), consistent with previous reports (*55*, *56*, *58*). The NMR spectrum observed in the presence of Dasatilink-1 closely matched the spectrum observed with a mixture of the two nonlinked inhibitors (fig. S8, A and B), suggesting that the linked inhibitor simultaneously binds to both sites and that the tether does not prevent binding to either site.

We hypothesized that DasatiLink-1 might require an allosteric foothold to achieve high occupancy of the BCR-ABL1 kinase domain, and we tested this hypothesis using a pull-down assay for ATP site availability (*59*). We confirmed that the assay recapitulated a biochemical IC_{50} of <1 nM for dasatinib (*60*), which was unaffected by inclusion of 100-fold excess of the allosteric inhibitor asciminib (fig. S8C). However, addition of excess asciminib impaired the ability of DasatiLink-1 to occupy the ATP site, likely resulting from a loss of avidity following steric occlusion of the allosteric pocket (fig. S8C). This indicates that

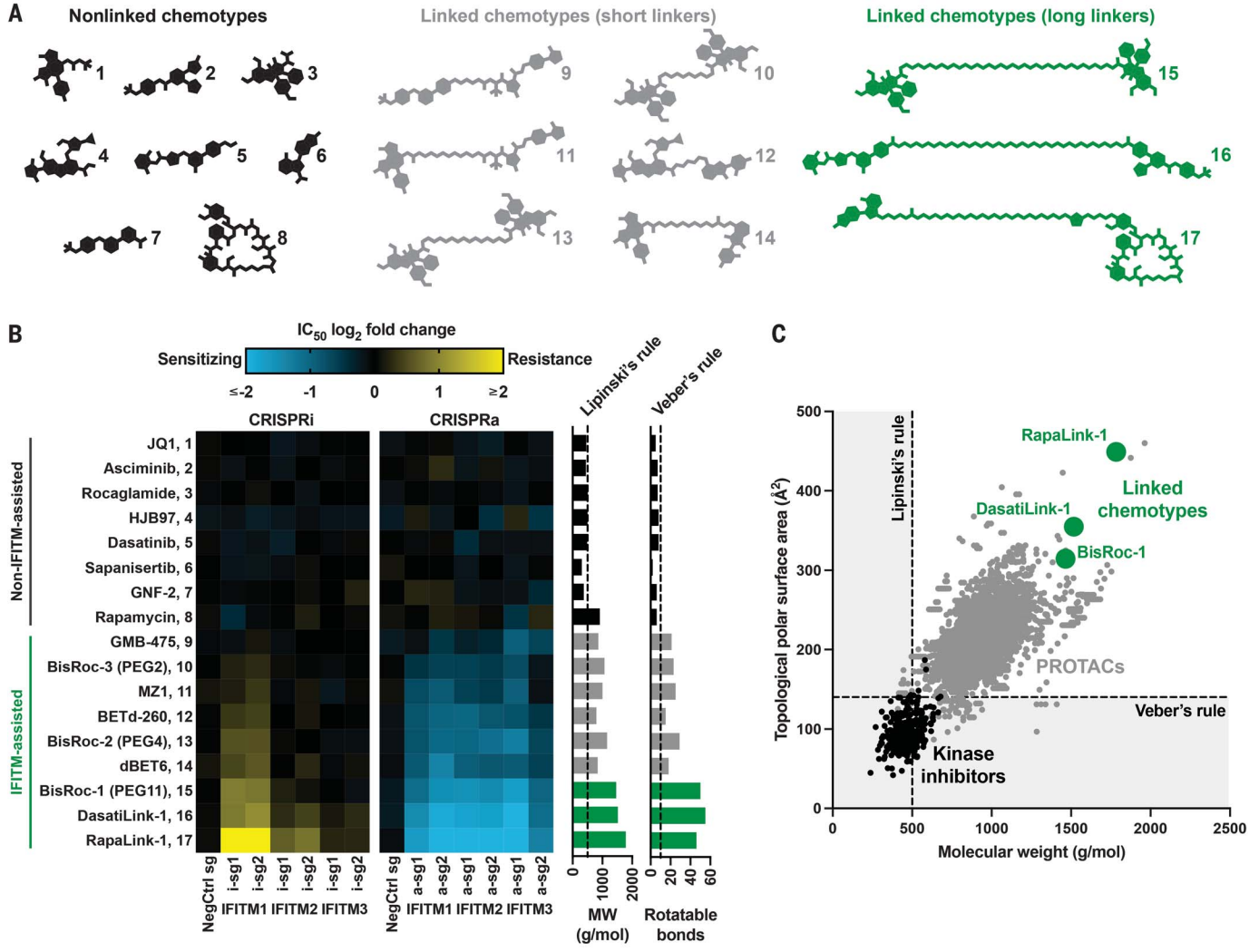

Fig. 4. IFITMs assist the cellular activity of diverse linked chemotypes. (**A**) Heavy atom skeletons of compounds assessed for IFITM assistance (see also fig. S10 for chemical structures). Compounds were categorized as nonlinked chemotypes (compounds 1 to 8, black), linked chemotypes with short linkers (compounds 9 to 14, gray), or linked chemotypes with long linkers (compounds 15 to 17, green). (**B**) Chemical-genetic interaction map of inhibitors in (A) with *IFITM1*, *IFTM2*, and *IFITM3*. Potency, as measured by dose-response IC_{50} in a cell viability assay (see also Fig. 1F, Fig. 3D, or fig. S9D for example source data), was normalized to that of non-sgRNA–expressing K562 CRISPRi or CRISPRa cells. Physicochemical properties, including molecular weight (MW) and number of rotatable bonds, with their respective traditional thresholds for drug-likeness are indicated (right). Data represent means of three biological replicates. (**C**) Map of chemical space populated by 304 kinase inhibitors in clinical development (black), 3270 PROTACs reported in the literature (gray), and 3 linked chemotypes described herein (green). Boundaries represent traditional guidelines for drug-likeness.

Dasatilink-1 relies on both the orthosteric and allosteric sites for binding, suggesting that it might also exhibit the enhanced selectivity often observed in bitopic inhibitors (*61*). Together, these biochemical data validate DasatiLink-1 as a bitopic inhibitor with physicochemical properties beyond standard drug design limits (*1*–*3*), and we reasoned that the molecule's linked composition might allow it to be assisted into the cell by IFITMs.

Returning to our K562 CRISPRi/a models, which are patient-derived BCR-ABL1 mutant CML cells, we characterized the effect of IFITM expression on the ability of DasatiLink-1 to inhibit intracellular BCR-ABL1 signaling. Similar to RapaLink-1 (Fig. 1, E and F), CRISPRi and CRISPRa perturbation of IFITM expression resulted in a combined 8.9-fold modulation of DasatiLink-1 cellular potency (Fig. 3, C and D). We also probed the capacity of DasatiLink-1 to engage intracellular BCR-ABL1 by measuring pharmacodynamic markers of inhibition. Consistent with an IFITM-assisted uptake mechanism, *IFITM1-3* triple knockdown reduced the ability of DasatiLink-1 to inhibit phospho-BCR-ABL1^{Y245} and phospho-STAT5^{Y694}, which are markers of BCR-ABL1 activity (Fig. 3E). The maximal inhibition observed for DasatiLink-1 in the TriNegCtrl sg conditions at 8 and 24 hours was not ever reached in the *IFITM1-3* triple knockdown conditions, likely due to lower intracellular concentrations of compounds resulting from decreased uptake. The inhibition kinetics we observed for the negative control treatment, requiring multiple hours for maximal inhibition at a nanomolar concentration (Fig. 3E), were also exhibited by RapaLink-1 (Fig. 1D).

We anticipated that DasatiLink-1, akin to RapaLink-1, was likely to be selective for its target as a result of its multivalent binding mechanism—only BCR-ABL1 kinase domain contains binding sites for both of its linked components. We assessed DasatiLink-1's kinome-wide selectivity in live cells using a

promiscuous kinase occupancy probe, XO44 (*62*), with which kinase active site occupancy can be determined through competitive activity-based protein profiling (*63*). In contrast to an unlinked control (a 1:1 mixture of dasatinib and asciminib) at equimolar concentration, which competed with XO44 for labeling of numerous known dasatinib targets (*62*), pretreatment with DasatiLink-1 resulted in observable intracellular occupancy of only ABL1 (Fig. 3F and data S6). This single kinase specificity extended over a 100-fold concentration range up to 1 μM, the same range over which the unlinked control demonstrated dose-responsive occupancy of numerous off targets (Fig. 3G and data S6). These data suggest that target selectivity can be conferred by two-site binding, analogous to RapaLink-1's selectivity for MTOR complex 1 (*7*, *24*, *25*).

BisRoc-1 analogs reveal linker length dependency of IFITM-assisted cellular uptake

To further examine the breadth of linked chemotypes that might be assisted by IFITMs, we designed, synthesized, and characterized a new linked molecular glue inhibitor based on the natural product rocaglamide. Rocaglamide clamps the EIF4A1 helicase to 5′ untranslated regions (UTRs) of target mRNAs to inhibit the translation of downstream sequences (*64*). The crystal structure of the complex of rocaglamide, EIF4A1, and polypurine RNA (*65*) revealed that the molecule's amide points toward free solvent, near a symmetry mate (fig. S9A). We reasoned that dimerization of rocaglamide through its amide position could be a chemically tractable means to simultaneously engage two proximal EIF4A1-RNA complexes within the cell. We designed a molecule, BisRoc-1 (fig. S9B), that links two rocaglamide monomers together with a linker length (35 heavy atoms) exceeding the distance separating two rocaglamide binding sites in the crystal structure (fig. S9A). Similar to RapaLink-1 and DasatiLink-1, CRISPRi and CRISPRa perturbation of IFITM expression resulted in a combined 6.2-fold modulation in cellular activity of BisRoc-1 (fig. S9, C and D). Additionally, we evaluated the relationship between linker length and IFITM assistance by examining an analog series consisting of BisRoc-1 (PEG11), BisRoc-2 (PEG4), BisRoc-3 (PEG2), and rocaglamide (no linker) (fig. S9E). We treated our K562 CRISPRi and CRISPRa cells with these inhibitors and evaluated differences in potency resulting from IFITM expression modulation, as measured by a half-maximal inhibitory concentration (IC_{50}) shift in a cell viability assay (fig. S9, E and F, and data S7). This revealed a pattern in which longer linker lengths correlated with greater IFITM assistance. Combined, these data suggest the general feasibility of retaining cell permeability despite increased pharmacophore size, polarity, and flexibility in the context of linked chemotypes described herein.

An expanded chemical space for cell-permeable molecules

Given the ubiquitous presence of IFITMs in cells, we hypothesized that the cellular uptake of other linked inhibitors in the literature could also be assisted by IFITMs. Although generally not as large as the linked chemotypes described above, PROTACs are likewise composed of two chemical entities covalently attached by a flexible tether (*16*). Thus, we included four PROTACs (GMB-475, MZ1, BETd-260, and dBET6) and their nonlinked parent inhibitors in an expanded survey of chemical-genetic interactions with IFITMs (Fig. 4A, fig. S10, and table S1). These compounds were evaluated in the same IFITM dependency analysis as the BisRoc linker series (Fig. 4B and data S7). Using RapaLink-1 as a chemical benchmark, we observed that *IFITM1*, *IFITM2*, and *IFITM3* overexpression sensitized cells to linked chemotypes (Fig. 4B; compounds 9 to 17). The inverse finding—resistance to linked chemotypes—resulted from gene knockdown (Fig. 4B). The trend observed in the BisRoc series was corroborated across the nine bivalent molecules tested (Fig. 4B): the magnitudes of chemical-genetic interactions correlated with linker length which is reflected in inhibitor size (molecular weight) and flexibility (number of rotatable bonds). Linked chemotypes with long linkers were more IFITM-assisted than linked chemotypes with short linkers, and nonlinked chemotypes (Fig. 4B; compounds 1 to 8) were not observed to be assisted by IFITMs (Fig. 4B). Despite their cellular activities, the physicochemical properties of the linked chemotypes largely violate Lipinski's (*1*) and Veber's (*2*) classic guidelines (Fig. 4, A to C, and table S1), raising the need for a revised drug design framework that considers IFITM-assisted uptake and other cellular import processes.

Discussion

Through a combination of functional genomics and chemical methods, we uncovered an endogenous pathway involving IFITMs that, in our data, promotes the cellular uptake of diverse linked chemotypes. With the clinical advancement of a dimeric immunophilin ligand (*23*), PROTACs (*16*), and a RapaLink-1 derivative (*26*), the notion of "drug-like" is continually being revised. As evidence, the chemical space (*66*) populated by an ever-expanding set of linked preclinical compounds in the literature ventures beyond that occupied by lead inhibitors developed under traditional guidelines (Fig. 4C) (*1*–*3*). Here, we identify IFITM-assisted cellular uptake as one of the mechanisms by which linked inhibitors are able to break previously established rules surrounding drug likeness. We anticipate that our findings will inform the uptake optimization of emerging classes of bivalent molecules (PROTACs, Syn-TEFs, RIBOTACs, PHICS, DUBTACs, and others) (*4*–*11*) and enable the design of cell-permeable therapeutics that bridge distal binding sites on solitary targets or multitarget complexes.

REFERENCES AND NOTES

1. C. A. Lipinski, F. Lombardo, B. W. Dominy, P. J. Feeney, *Adv. Drug Deliv. Rev.* **46**, 3–26 (2001).
2. D. F. Veber *et al.*, *J. Med. Chem.* **45**, 2615–2623 (2002).
3. A. K. Ghose, V. N. Viswanadhan, J. J. Wendoloski, *J. Comb. Chem.* **1**, 55–68 (1999).
4. M. Erez, A. E. Takemori, P. S. Portoghese, *J. Med. Chem.* **25**, 847–849 (1982).
5. D. M. Spencer, T. J. Wandless, S. L. Schreiber, G. R. Crabtree, *Science* **262**, 1019–1024 (1993).
6. K. M. Sakamoto *et al.*, *Proc. Natl. Acad. Sci. U.S.A.* **98**, 8554–8559 (2001).
7. V. S. Rodrik-Outmezguine *et al.*, *Nature* **534**, 272–276 (2016).
8. G. S. Erwin *et al.*, *Science* **358**, 1617–1622 (2017).
9. M. G. Costales, Y. Matsumoto, S. P. Velagapudi, M. D. Disney, *J. Am. Chem. Soc.* **140**, 6741–6744 (2018).
10. S. U. Siriwardena *et al.*, *J. Am. Chem. Soc.* **142**, 14052–14057 (2020).
11. N. J. Henning *et al.*, *Nat. Chem. Biol.* **18**, 412–421 (2022).
12. B. C. Doak, B. Over, F. Giordanetto, J. Kihlberg, *Chem. Biol.* **21**, 1115–1142 (2014).
13. M. Green, P. M. Loewenstein, *Cell* **55**, 1179–1188 (1988).
14. A. D. Frankel, C. O. Pabo, *Cell* **55**, 1189–1193 (1988).
15. E. L. Snyder, S. F. Dowdy, *Pharm. Res.* **21**, 389–393 (2004).
16. M. Békés, D. R. Langley, C. M. Crews, *Nat. Rev. Drug Discov.* **21**, 181–200 (2022).
17. C. A. Foley, F. Potjewyd, K. N. Lamb, L. I. James, S. V. Frye, *ACS Chem. Biol.* **15**, 290–295 (2020).
18. C. Cantrill *et al.*, *Drug Discov. Today* **25**, 969–982 (2020).
19. D. E. Scott *et al.*, *ACS Med. Chem. Lett.* **11**, 1539–1547 (2020).
20. G. Ermondi, M. Vallaro, G. Caron, *Drug Discov. Today* **25**, 1585–1591 (2020).
21. V. G. Klein *et al.*, *ACS Med. Chem. Lett.* **11**, 1732–1738 (2020).
22. Y. Atilaw *et al.*, *ACS Med. Chem. Lett.* **12**, 107–114 (2020).
23. A. D. Stasi *et al.*, *N. Engl. J. Med.* **365**, 1673–1683 (2011).
24. Q. Fan *et al.*, *Cancer Cell* **31**, 424–435 (2017).
25. B. J. Lee *et al.*, *Nat. Chem. Biol.* **17**, 1065–1074 (2021).
26. H. A. Burris III *et al.*, *J. Clin. Oncol.* **40**, 3098 (2022).
27. Z. Zhang *et al.*, *Nature* **609**, 822–828 (2022).
28. L. A. Gilbert *et al.*, *Cell* **159**, 647–661 (2014).
29. M. A. Horlbeck *et al.*, *eLife* **5**, e19760 (2016).
30. M. Jost *et al.*, *Mol. Cell* **68**, 210–223.e6 (2017).
31. M. Jost, J. S. Weissman, *ACS Chem. Biol.* **13**, 366–375 (2018).
32. G. Y. Liu, D. M. Sabatini, *Nat. Rev. Mol. Cell Biol.* **21**, 183–203 (2020).
33. E. De Zan *et al.*, *Sci. Signal.* **13**, eaba5665 (2020).
34. K. J. Condon *et al.*, *Proc. Natl. Acad. Sci. U.S.A.* **118**, e2022120118 (2021).
35. Z. Zhang, J. Liu, M. Li, H. Yang, C. Zhang, *PLOS ONE* **7**, e49265 (2012).
36. P. Li *et al.*, *Biochim. Biophys. Acta Gene Regul. Mech.* **1860**, 885–893 (2017).
37. M. J. Garnett *et al.*, *Nature* **483**, 570–575 (2012).
38. M. G. Rees *et al.*, *Nat. Chem. Biol.* **12**, 109–116 (2016).
39. F. Iorio *et al.*, *Cell* **166**, 740–754 (2016).
40. B. Adamson *et al.*, *Cell* **167**, 1867–1882.e21 (2016).
41. B. R. Stockwell, *Nat. Rev. Genet.* **1**, 116–125 (2000).

42. A. L. Brass *et al*., . *Cell* **139**, 1243–1254 (2009).
43. C. C. Bailey, G. Zhong, I.-C. Huang, M. Farzan, *Annu. Rev. Virol.* **1**, 261–283 (2014).
44. G. Shi, O. Schwartz, A. A. Compton, *Retrovirology* **14**, 53 (2017).
45. X. Zhao, J. Li, C. A. Winkler, P. An, J.-T. Guo, *Front. Microbiol.* **9**, 3228 (2019).
46. K. Li *et al*., *PLOS Pathog.* **9**, e1003124 (2013).
47. X. Zhao *et al*., *Proc. Natl. Acad. Sci. U.S.A.* **111**, 6756–6761 (2014).
48. J. Lee *et al*., *Nature* **588**, 491–497 (2020).
49. J. Buchrieser *et al*., *Science* **365**, 176–180 (2019).
50. J. S. Spence *et al*., *Nat. Chem. Biol.* **15**, 259–268 (2019).
51. T. Das *et al*., *ACS Chem. Biol.* **17**, 2109–2120 (2022).
52. R. Kurzrock, J. U. Gutterman, M. Talpaz, M. Talpaz, *N. Engl. J. Med.* **319**, 990–998 (1988).
53. T. Schindler *et al*., *Science* **289**, 1938–1942 (2000).
54. T. P. Braun, C. A. Eide, B. J. Druker, *Cancer Cell* **37**, 530–542 (2020).
55. J. Zhang *et al*., *Nature* **463**, 501–506 (2010).
56. A. A. Wylie *et al*., *Nature* **543**, 733–737 (2017).
57. R. E. Iacob, J. Zhang, N. S. Gray, J. R. Engen, *PLOS ONE* **6**, e15929 (2011).
58. N. Vajpai *et al*., *J. Biol. Chem.* **283**, 18292–18302 (2008).
59. M. A. Fabian *et al*., *Nat. Biotechnol.* **23**, 329–336 (2005).
60. J. Das *et al*., *J. Med. Chem.* **49**, 6819–6832 (2006).
61. C. M. Gower, M. E. K. Chang, D. J. Maly, *Crit. Rev. Biochem. Mol. Biol.* **49**, 102–115 (2014).
62. Q. Zhao *et al*., *J. Am. Chem. Soc.* **139**, 680–685 (2017).
63. B. F. Cravatt, A. T. Wright, J. W. Kozarich, *Annu. Rev. Biochem.* **77**, 383–414 (2008).
64. S. Iwasaki, S. N. Floor, N. T. Ingolia, *Nature* **534**, 558–561 (2016).
65. S. Iwasaki *et al*., *Mol. Cell* **73**, 738–748.e9 (2019).
66. C. M. Dobson, *Nature* **432**, 824–828 (2004).
67. D. R. Wassarman, dwassarman/cellpanelr, v0.0.0.9001, Zenodo (2022).
68. M. A. Horlbeck, X. Xiong, M. Jost, mhorlbeck/ScreenProcessing, v0.1, Zenodo (2022).

ACKNOWLEDGMENTS

Sequencing was performed at the UCSF CAT, supported by UCSF PBBR, RRP IMIA, and NIH 1S10OD028511-01 grants. We thank T. S. Wu for computational advice, S. Kim and K. Herrington at the UCSF Nikon Imaging Center for their microscopy assistance and expertise, D. M. Peacock for assistance acquiring NMR characterization of compounds synthesized herein, and J. W. Stevenson for proofreading. **Funding:** This work was supported by NIH grant F30CA239476 (to K.L.); NIH grant F31CA243439 (to D.R.W.); Damon Runyon Cancer Research Foundation fellowship DRG-2281-17 (to Z.Z.); Wellcome Trust grant 102696 (to C.H.B.); NIH grant R35GM119437 (to M.A.S.); Ono Pharma Foundation and Pfizer (to J.T.); NIH New Innovator Award DP2-CA239597, a Pew-Stewart Scholars for Cancer Research award, and the Goldberg-Benioff Endowed Professorship in Prostate Cancer Translational Biology (to L.A.G.); the Howard Hughes Medical Institute, the Samuel Waxman Cancer Research Foundation, and NIH grants 1R01CA221969 and 1U19 AI171110-01 (to K.M.S.). **Author contributions:** K.L., L.A.G., and K.M.S. were responsible for the conception, design, and interpretation of the experiments and wrote the manuscript. K.L. performed CRISPRi/a experiments, cellular uptake assays, and chemical-genetic interaction mapping. K.L. designed and synthesized DasatiLink and BisRoc molecules. D.R.W., R.K.E., and P.G. performed sensitivity-expression correlation experiments. T.Y. performed chemoproteomic kinase target engagement assays. Y.P. performed protein NMR spectroscopy. Z.Z. designed and synthesized TAMRA molecules. T.A.O. performed fluorescent microscopy experiments. M.K.M. performed biological validation of BisRoc experiments. C.H.B., M.A.S., J.T., L.A.G., and K.M.S. supervised experiments and interpreted data. All authors edited the manuscript. **Competing interests:** K.L. and K.M.S. have filed a patent application covering DasatiLink analogs. K.L., M.K.M., and K.M.S. have filed a patent application covering BisRoc analogs. Kin of K.L. hold stock in and are employed by Pharmaron. C.H.B. is currently an employee of Novartis. J.T. is a founder of Global Blood Therapeutics, Principia Biopharma, Kezar Life Sciences, Cedilla Therapeutics, and Terremoto Biosciences, and is a scientific advisor to Entos. L.A.G. has filed patent applications related to CRISPRi/a screening. K.M.S. has filed patent applications covering RapaLink analogs which are licensed to Revolution Medicines. K.M.S. receives stock and cash compensation from Revolution Medicines. **Data and materials availability:** All data are available in the manuscript or the supplementary materials. Scripts implementing analyses are available at https://github.com/dwassarman, https://github.com/mhorlbeck, and Zenodo (*67*, *68*). Materials are available upon request to the corresponding authors with a signed material transfer agreement. This article is subject to HHMI's Open Access to Publications policy. HHMI lab heads have previously granted a nonexclusive CC BY 4.0 license to the public and a sublicensable license to HHMI in their research articles. Pursuant to those licenses, the author-accepted manuscript of this article can be made freely available under a CC BY 4.0 license immediately upon publication.

SUPPLEMENTARY MATERIALS

science.org/doi/10.1126/science.abl5829
Chemical Synthesis
Materials and Methods
Figs. S1 to S10
Tables S1 and S2
References (*69*–*77*)
MDAR Reproducibility Checklist
Data S1 to S7

Submitted 26 July 2021; resubmitted 5 May 2022
Accepted 19 October 2022
10.1126/science.abl5829

IFITM proteins assist cellular uptake of diverse linked chemotypes

Kevin Lou, Douglas R. Wassarman, Tangpo Yang, YiTing Paung, Ziyang Zhang, Thomas A. OLoughlin, Megan K. Moore, Regina K. Egan, Patricia Greninger, Cyril H. Benes, Markus A. Seeliger, Jack Taunton, Luke A. Gilbert, and Kevan M. Shokat

Science, **378** (6624), .
DOI: 10.1126/science.abl5829

Beyond traditional drug design

Drug design prioritizes compounds likely to cross the cell membrane, leading to rules governing the size, polarity, and rigidity of chemical structures. However, there is increased interest in linking two chemotypes to allow greater selectivity for one target or to associate two targets. Lou *et al*. focused on a bitopic inhibitor, Rapalink-1, of the signaling protein mTOR that is active in vivo even though it is much too large to be considered drug like (see the Perspective by Lokey and Pye). The authors used chemical genetic approaches to show that the activity of Rapalink-1 depends on interferon-induced transmembrane proteins (IFITMs). They went on to show that IFITMs promote the cellular uptake of diverse linked chemotypes and to explore the role of linker length on the uptake pathway. This work may guide the development of bitopic drugs. —VV